# Diel Cycle Impacts on the Chemical and Light Absorption Properties of Organic Carbon Aerosol from Wildfires in the Western United States

Benjamin Sumlin[1], Edward Fortner[2], Andrew Lambe[2], Nishit J. Shetty[1], Conner Daube[2], Pai Liu[1], Francesca Majluf[2], Scott Herndon[2], and Rajan K. Chakrabarty[1]

[1]Center for Aerosol Science and Engineering, Department of Energy, Environmental, and Chemical Engineering, Washington University in St. Louis, St. Louis, Missouri
[2]Aerodyne Research, Inc., Billerica, Massachusetts

*Correspondence to*: Benjamin Sumlin (bsumlin@wustl.edu) and Rajan K. Chakrabarty (chakrabarty@wustl.edu)

**Abstract.** Organic aerosol (OA) emissions from biomass burning have been the subject of intense research in recent years, involving a combination of field campaigns and laboratory studies. These efforts have aimed at improving our limited understanding of the diverse processes and pathways involved in the atmospheric processing and evolution of OA properties, culminating in their accurate parameterizations in climate and chemical transport models. To bring closure between laboratory and field studies, wildfire plumes in the western United States were sampled and characterized for their chemical and optical properties during the ground-based segment of the 2019 Fire Influence on Regional to Global Environments and Air Quality (FIREX-AQ) field campaign. Using a custom-developed multiwavelength integrated photoacoustic-nephelometer spectrometer in conjunction with a suite of instruments, including an oxidation flow reactor equipped to generate hydroxyl (OH·) or nitrate (NO$_3$·) radicals to mimic daytime or nighttime oxidative aging processes, we investigated the effects of multiple equivalent hours of OH·/NO$_3$· exposure on the chemical composition and mass absorption cross-sections (MAC($\lambda$)) at 488 and 561 nm of OA emitted from wildfires in Arizona and Oregon. We found that OH· exposure induced a slight initial increase in absorption corresponding to short timescales, however, in longer time scales, the wavelength-dependent MAC($\lambda$) decreased by a factor of $0.72 \pm 0.08$, consistent with previous laboratory studies and reports of photobleaching. On the other hand, NO$_3$· exposure increased MAC($\lambda$) by a factor of up to $1.69 \pm 0.38$. We also noted some sensitivity of aerosol aging to different fire conditions between Arizona and Oregon. The MAC($\lambda$) enhancement following NO$_3$· exposure was found to correlate with an enhancement in CHO$_1$N and CHO$_{gt1}$N ion families measured by an Aerodyne aerosol mass spectrometer.

## 1 Introduction

Wildfires constitute one of the main contributions to the global atmospheric organic aerosol (OA) burden (Murphy et al., 2006; Zhang et al., 2007). The diverse physical, chemical, and optical properties of OA, the varied pathways involved in their formation in fires, and subsequent atmospheric processing introduce uncertainty into the analysis of their climate impacts, preventing extensive and accurate representation within regional and global scale models. Laboratory studies have, in the recent several years, demonstrated the effects of atmospheric processing on the optical,

chemical, and physical properties of biomass burning OA (BBOA) or secondary organic aerosol (SOA) from biomass sources (Jimenez et al., 2009; Kroll et al., 2011; Lambe et al., 2013; Sumlin et al., 2017a). BBOA is typically also associated with brown carbon (BrC), a class of OA known to strongly absorb sunlight in the UV and short visible wavelengths (Pósfai et al., 2004; Chakrabarty et al., 2010). Following diurnal cycles, the impacts of atmospheric oxidation can be broadly divided into daytime- and nighttime-driven processes. During daylight hours, the dominant oxidant that may influence OA properties is OH·. At night, when OH· production is significantly lower, $O_3$ or $NO_3$· are the most likely oxidants to influence biomass burning OA (BBOA) properties. Initial laboratory studies suggest OH· and $NO_3$·-induced oxidative aging affect the light absorption properties of BBOA surrogates in markedly different ways. OH· exposure to diminish light absorption by fragmenting large chromophoric molecules (Lambe et al., 2013; Sumlin et al., 2017a), while $NO_3$· oxidation has been shown to enhance light absorption by adding nitrogen-containing chromophoric functional groups (Li et al., 2019; Cheng et al., 2020; Li et al., 2020; He et al., 2021).

The need to study the consequences of such atmospheric processing on BBOA has motivated the development and use of environmental chambers capable of containing and controlling a sample of aerosol as it ages naturally (such as a Teflon bag sitting in open sunlight) or by accelerating the aging process by exposing aerosols to increased concentrations of atmospheric oxidants, UV light, or both (Carter et al., 1995; Cocker et al., 2001; Grieshop et al., 2009; Cubison et al., 2011; Ortega et al., 2013). Such chambers are often large, on the order of several cubic meters (Cocker et al., 2001), and the relatively slow pace of a given experiment may suffer from unrealistic loss mechanisms including wall losses (including electrostatic, diffusional, and gravitational) (McMurry and Grosjean, 1985; Zhang et al., 2014; Wang et al., 2018) and aerosol agglomeration and coagulation (Pierce et al., 2008). Recently, oxidation flow reactors (OFRs) have been used as a field-deployable alternative to traditional environmental chambers. OFRs are comparatively small, on the order of 0.01 $m^3$, with residence times on the order of minutes and oxidant concentrations that are 100-1000 times higher than typical ambient levels, resulting in equivalent atmospheric aging time scales from hours to weeks (Lambe et al., 2011).

While most work with OFRs has focused on OH·-initiated oxidative aging processes, new methods are available to employ $NO_3$· in field-based OFR studies (Lambe et al., 2020; Li et al., 2020) that expand on previous work (Palm et al., 2017). The consequences of such atmospheric processing over multiple diurnal cycles and broad geographical areas introduce significant errors into the aerosol components of radiative transfer models and make it difficult to constrain the impacts that wildfires and other large-scale aerosol events will have on the climate, especially in areas where air quality is expected to suffer under the effects of anthropogenic climate change (McClure and Jaffe, 2018).Following previous laboratory studies that investigated the various properties of BrC generated from smoldering biomass (Sumlin et al., 2017b; Sumlin et al., 2018a; Sumlin et al., 2018b), including their optical characteristics following OH· exposure in an OFR , this work investigates the effects of daytime and nighttime aging on the short visible wavelength-dependent light absorbing properties of smoke OA sampled during the Fire Influence on Regional to Global Environments and Air Quality (FIREX-AQ) campaign, an interagency mission led by NASA and NOAA, conducted during the wildfire season of 2019 (Warneke, in preparation). This work focuses on four OFR-based OA oxidative aging experiments performed in August 2019 at ground level near the North Rim of the Grand Canyon in

Arizona during the Castle and Ikes fires, and in Eastern Oregon, during the 204 Cow Fire. Results are used to quantify the effects of diurnal cycle-driven oxidation processes on the OA mass absorption cross-section.

**2 Methods**

**2.1 Wildfire emissions sampled during OFR experiments**

65 **2.1.1 Castle and Ikes Fires, Northern Arizona**

At the time of the FIREX-AQ campaign, two large fires were burning in close proximity to each other near the North Rim of the Grand Canyon, near Page, AZ. These fires, the Castle and Ikes fires (36.51° N, 112.28° W, and 36.35° N, 112.29° W, respectively), were ignited by lightning on 12 and 25 July 2019, respectively, by lightning strikes. Since these fires threatened no structures or other property and were burning through a forest densely packed with litter,
70 underbrush, and dead fallen trees, the fires were allowed to burn within prescribed limits to serve their role as the forest's natural mechanism of cleanout and renewal while fire crews in the area used Castle and Ikes as training opportunities.

The Castle and Ikes fires burned near the Oquer Canyon in the Kaibab National Forest, a densely forested area consisting predominantly of Ponderosa pine (*Pinus ponderosa*), Douglas fir (*Pseudotsuga menziesii*), Englemann
75 spruce (*Picea engelmannii*), and quaking aspen (*Populus tremuloides*). Minor species include Gambel oak (*Quercus gambelii*), and various shrub and grass species of sagebrush (*Artemesia*) and bitterbrush (*Purshia*). A complete description of the fuel bed in this region are given in Appendix A of Riccardi et al. (2007). By 20 August 2019, the fire management areas had grown to approximately 24,000 acres (~97 km$^2$) combined. The Aerodyne Mobile Laboratory (AML, described below) approached from Page via Highway 89A and State Route 67. An OH·-OFR
80 experiment (OH$_{Arizona}$) was conducted on 20 August at approximately 17:45 UTC (10:45 MST) at 36.61°N, 112.19°W (Fig. 1), and a NO$_3$·-OFR experiment (NO$_{3,Arizona}$) was conducted on 22 August at approximately 10:30 UTC (03:30 MST) at 36.54° N, 112.17° W (Fig. 2).

[Figure 1]

[Figure 2]

85

**2.1.2 204 Cow Fire, Eastern Oregon**

After returning from Arizona, the nearest fire of interest was the 204 Cow Fire (44.28° N, 118.47° W) in the Malheur National Forest region of the Blue Mountains in eastern Oregon, approximately 200 km west-southwest of McCall. The 204 Cow Fire was ignited on 9 August by lightning and grew to burn 9,668 acres (approximately 29 km$^2$) until
90 its containment on 15 October. The region is predominantly forested by various species of pine, fir, and juniper trees (*Pinus*, *Abies*, and *Juniperus*, respectively) along with shrub species of sagebrush (*Artemesia*) (Riccardi et al. 2007). The fire had burned approximately 5,500 acres (22.3 km$^2$) by 26 August, when both OH·-OFR ("OH$_{Oregon}$", 09:30 UTC, 03:30 MDT, 44.23° N, 118.40° W) and NO$_3$·-OFR ("NO$_{3,Oregon}$", 12:30 UTC, 06:30 MDT, 44.25° N, 118.40°

W) experiments took place (Fig. 3). The AML approached from State Route 26 and then traversed a series of National
95 Forest Development roads to conduct sampling less than 3 km from the fire management area.

[Figure 3]


[Figure 4]


100 **2.2 Instrumentation**

**2.2.1 Multiwavelength Integrated Photoacoustic-Nephelometer (MIPN)**

A description of the design and development of this instrument, including calibration procedures, has been given previously (Arnott et al., 1999; Arnott et al., 2000; Moosmüller and Arnott, 2003; Varma et al., 2003; Lewis et al., 2008). Briefly, the aerosol light absorption coefficient ($\beta_{abs}$, Mm$^{-1}$) was measured with the prototype version of a new
105 Multiwavelength Integrated Photoacoustic-Nephelometer (MIPN) at two wavelengths ($\lambda$ = 488 and 561 nm). The MIPN is based upon single-wavelength instruments constructed at Washington University in St. Louis and described previously (Sumlin et al., 2017a; Sumlin et al., 2018a; Sumlin et al., 2018b). Novel to the MIPN is a dual-cell arrangement wherein the sample stream is split and one branch is filtered to remove particulate matter, thereby simultaneously sampling a particle-free gaseous background to account for noise from various sources such as ambient
110 acoustic, electrical, and flow noise. Data were acquired from each wavelength in serial at 0.5 Hz for one minute per wavelength and averaged across each wavelength's one-minute cycle. Due to a field malfunction, scattering measurements were not obtained.

OA mass absorption cross-sections (MAC($\lambda$), m$^2$ g$^{-1}$) at the two operating wavelengths were calculated from the ratio of $\beta_{abs}$ measured with MPIN and OA mass concentrations measured with the SP-AMS after correcting for dilution and
115 wall losses in the OFR. We additionally calculated the MAC($\lambda$) enhancement, $E_{MAC}(\lambda)$, from the ratio of OFR-processed and ambient MAC($\lambda$) values. Thus, $E_{MAC}(\lambda)$ > 1 indicates an oxidative aging-induced absorption enhancement, while $E_{MAC}(\lambda)$ < 1 indicates diminished absorption. To obtain reasonable estimates for $E_{MAC}(\lambda)$ values that are comprehensive of a given oxidation step yet still capture the nature of the dynamic plume, $E_{MAC}(\lambda)$ was calculated using the average of aerosol MAC($\lambda$) during a given oxidation step divided by the average of the ambient
120 steps immediately prior and after.


**2.2.2 Aerosol Mass Spectrometer**

The SP-AMS is a standard Aerodyne high resolution time of flight aerosol mass spectrometer (HR-ToF-AMS) with an intracavity, CW laser vaporizer (Onasch et al., 2012). The AMS was operated to provide online chemically-speciated mass and sizing measurements of both non-refractory and refractory particles between approximately 70 –
125 2500 nm in aerodynamic diameter. A PM$_{2.5}$ inlet lens was installed on the AMS for this study, extending the range of 100% transmission efficiency of particles through the lens up to 2.5 µm in diameter. The SP-AMS laser was operated with approximately a 50% duty cycle. When the laser was off, the system was operated as a conventional AMS. During OH$_{Arizona}$, OH$_{Oregon}$, and NO$_{3,Oregon}$, the SP-AMS was used. During NO$_{3,Arizona}$, the conventional AMS was used.

The instrument was run with 20 second time resolution, and data points included both chemical speciation and mass loading by mass spectral analysis and particle sizing by species for each data point. In the SP-AMS, particles containing refractory materials (i.e. rBC and many metals) are vaporized with a 1064 nm laser. The resulting vapor is ionized via electron impact and detected with the HR-TOF-AMS. In addition to the SP-AMS vaporization, the conventional AMS heater (a heated tungsten surface at 600 °C, (Jayne et al., 2000; Canagaratna et al., 2007) was also used to measure the composition of any non-refractory particles. When the instrument was run as a conventional AMS, this was the only heater used.

### 2.2.3 Potential Aerosol Mass Oxidation Flow Reactor (OFR)

The Potential Aerosol Mass OFR (Aerodyne Research, Inc.; Lambe et al., 2011) is a horizontal 13 L aluminum cylindrical chamber (46 cm long × 22 cm ID) operated in continuous flow mode. Irradiance, relative humidity and temperature in the OFR were measured at the exit flange with UV (TOCON GaP6, sglux) and RH/T (SHT21, Sensiron) sensors, and ozone concentrations were measured with an ozone analyzer (Model 106-M, 2B Technologies).

### 2.2.4 Aerodyne Mobile Laboratory

The AML, a mobile sampling platform equipped with a suite of research-grade instrumentation, was used to facilitate the in situ OFR-based experiments described here. The AML travelled throughout Idaho, Oregon, Utah, and Arizona during FIREX-AQ, sampling continuously when not conducting OFR experiments. The general sampling strategy was to search for smoke-filled valleys and transect plumes with the AML, using Tuneable Infrared Laser Direct Absorption Spectrometer (TILDAS, Aerodyne Research, Inc.) (McManus et al., 2011a; McManus et al., 2011b) measurements of hydrogen cyanide (HCN) as a tracer for biomass smoke plumes (Li et al., 2000). Upon identification of a suitable location, the AML parked with the sample inlet on the front of the truck facing into the wind to avoid self-sampling of its own exhaust. A $PM_{2.5}$ cyclone with a small mesh screen to filter out extremely large ash particles was attached to the inlet. A schematic of the OFR experimental setup is given in Fig. 4.

AML positioning, including latitude, longitude, and altitude was measured by a Vector V103 GPS Compass (Hemisphere GNSS, Inc., Scottsdale, AZ). Wind velocity was measured by an ultrasonic anemometer (model 86000, R. M. Young Company, Traverse City, MI). Additional meteorology products were obtained from the NOAA Air Resources Laboratory North American Mesoscale 12 km Archive, and plume ages were approximated using the Hybrid Single-Particle Lagrangian Integrated Trajectory (HYSPLIT) model (Stein et al., 2016). Aerosol composition and mixing state properties were measured with a Soot Particle Aerosol Mass Spectrometer (SP-AMS, Aerodyne Research, Inc., Onasch et al., 2012) and Single Particle Soot Photometer (SP2 Droplet Measurement Technologies, Stephens et al., 2003). A Vocus Proton Transfer Reaction Mass Spectrometer (Krechmer et al., 2018) (PTR-MS, Aerodyne Research, Inc./Tofwerk AG, Switzerland ) sampled VOCs.

### 2.3 Experiment Design

The total instrument plus makeup flowrate through the OFR was 6.4 liter min$^{-1}$, corresponding to a calculated mean plug flow residence time of 123 sec. The degree to which plug flow is a valid model for an OFR is the subject of ongoing research, however, this assumption is adequate for the flowrates and experimental setups used here (Mitroo et al. 2018). OFR experiments lasted 1 to 2 hours, during which the reagent inputs were controlled in steps to simulate varying degrees of atmospheric aging. An experiment step consists of two phases, an ambient phase and a reaction phase. During the ambient phase, instruments first sampled ambient air for 5-10 min (depending on the experiment timeline) while LFR/OFR conditions equilibrated for the reaction phase. During the ambient phase, 5 L min$^{-1}$ of makeup flow was pulled through the OFR to reduce stagnation time. Once the ambient phase ended, an electronically actuated 3-way valve was switched to connect the instruments to the OFR, and OFR-processed air was sampled for 5 to 10 min. After each step, the OH· or NO$_3$· exposure was changed, and the above measurements were repeated. After each experiment, the OFR was cleaned out by setting both sets of lamps to maximum output and overblowing the inlet with humidified zero air until AMS measurements of background organic mass were below 0.3 µg m$^{-3}$. To account for dilution and particle wall losses in the OFR refractory black carbon (rBC) monitored with the SP2 was used as a chemically conserved tracer. During all experiments, rBC accounted for ~ 2% to 5% of total aerosol mass (Figs. S1 and S2).

In the following sections, ambient phases are denoted "ambient_X" and oxidation phases are denoted "OFR_OH_X" for OH· experiments, and for NO$_3$· experiments, the ozone-only step is denoted "OFR_O3" and NO$_3$· oxidation steps are denoted "OFR_NO3_X". "X" indicates the step number. Finally, each experiment includes a "background" measurement, where ambient air was sampled through the dark OFR without oxidant generation.

### 2.3.1 NO$_3$ Experiment Design and Analysis

To generate NO$_3$·, N$_2$O$_5$ was first generated in the gas phase from the reaction NO$_2$ + O$_3$ → NO$_3$· + O$_2$ followed by the reaction NO$_3$· + NO$_2$ → N$_2$O$_5$ in a 152.4 cm long x 2.22 cm ID perfluoroalkoxy laminar flow reactor (LFR) coupled to the OFR (Lambe et al., 2020). Separate flows containing NO$_2$ (1% in N$_2$, Praxair) and O$_3$ were added to the LFR. In these experiments, the NO$_2$ +N$_2$ flow rate was set between 0 and 40 cm$^3$ min$^{-1}$, and O$_3$ was generated by passing 1.8 L min$^{-1}$ of O$_2$ through an ozone chamber housing a mercury fluorescent lamp (GPH212T5VH, Light Sources, Inc.). The O$_3$ mixing ratio that was input to the LFR was approximately 250 ppmv during NO$_3$·-OFR experiments. The NO$_2$ + N$_2$ and O$_2$ flow rates were set using mass flow controllers. The N$_2$O$_5$ generated in the LFR thermally decomposed at room temperature inside the OFR to generate NO$_3$·. The first oxidation step of NO$_3$·-OFR experiments was with ozone only ("OFR_O3") to assess the effect of O$_3$ exposure on OA composition and optical properties relative to ambient OA. During NO$_{3,Arizona}$, NO$_2$ was stepped down from 40 to 20, 5, and 3 cm$^3$ min$^{-1}$ to generate the various oxidation time scales (Fig. S3). During NO$_{3,Oregon}$, inputs of 15 and 5 cm$^3$ min$^{-1}$ were used. The integrated NO$_3$ exposure, defined as the product of the average NO$_3$· concentration and the mean OFR residence time ($\tau_{OFR}$), was calculated using an estimation equation developed by Lambe et al. (2020):
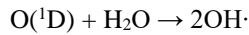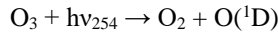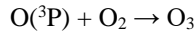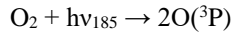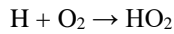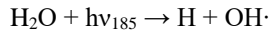
$$\log[(NO_3)_{exp}] = a + b \log[273.15 + T_{OFR}] + c \log[\tau_{OFR}]$$

$$+ d \log[NO_2]_{0,LFR} + e \log[O_3]_{0,LFR} \times T_{OFR} + f \log[k_{w_{OFR},N_2O_5}]$$

$$+ \log\left(\frac{[NO_2]_{0,LFR}}{[O_3]_{0,LFR}}\right) \times \left(g\left(\log[O_3]_{0,LFR}\right)^2 + h\log[O_3]_{0,LFR}\right)$$

$$- \frac{[NO_2]_{0,LFR}}{[O_3]_{0,LFR}} \times \left(i + j\log[O_3]_{0,LFR}\right) + k\log(NO_3R)_{ext}$$

$$+ l\log[NO_2]_{0,LFR} \times T + m\log[O_3]_{0,LFR} \times \log k_{w_{OFR,N_2O_5}} \qquad (1)$$

Where $a$ through $m$ are empirical fit coefficients derived by Lambe et al. (2020) and summarized in Table S1, $T_{OFR}$ is the measured temperature in the OFR, $[NO_2]_{0,LFR}$ and $[O_3]_{0,LFR}$ were the $NO_2$ and $O_3$ mixing ratios input to the LFR (ppmv), $k_{wOFR,N2O5} = 0.01$ s$^{-1}$ is the assumed $N_2O_5$ wall loss rate coefficient in the OFR, and $(NO_3R)_{ext}$ is the external $NO_3\cdot$ reactivity (s$^{-1}$), which was calculated from the summed products of ambient VOC concentrations (measured with Vocus) and their and their $NO_3\cdot$ rate coefficients (found in the data repository, see Data Availability section). Corresponding calculated $NO_3\cdot$ exposures ranged from $1.4\times10^{14}$ to $3.4\times10^{14}$ molec cm$^{-3}$ s, or approximately 72 to 192 equivalent hours (3 to 8 equivalent days) of atmospheric oxidation at a 24-hour average $NO_3\cdot$ concentration of $5\times10^8$ molec cm$^{-3}$ (Atkinson, 1991).

### 2.3.2 OH· Experiment Design

OH· was generated via photolysis of ambient $O_2$ and $H_2O$ at $\lambda = 185$ nm plus photolysis of $O_3$ (generated from at $\lambda = 254$ nm using low-pressure mercury (Hg) lamps):

$$H_2O + h\nu_{185} \rightarrow H + OH\cdot$$
$$H + O_2 \rightarrow HO_2$$
$$O_2 + h\nu_{185} \rightarrow 2O(^3P)$$
$$O(^3P) + O_2 \rightarrow O_3$$
$$O_3 + h\nu_{254} \rightarrow O_2 + O(^1D)$$
$$O(^1D) + H_2O \rightarrow 2OH\cdot$$

A fluorescent dimming ballast was used to regulate current applied to the lamps (GPH436T5VH/4, Light Sources, Inc.). The dimming voltage applied to the ballast ranged from 1.6 V to 10 V direct current (DC). To extend the range of OH· concentrations below what is achievable with one set of lamps at 1.6 VDC, a second set of GPH436T5VH/4 lamps with added segments of opaque heat shrink tubing applied to ~86 % of the arc length (Rowe et al., 2020) was used. The $OH_{Arizona}$ OFR experiment began with the non-attenuated lamps set to maximum output, then switching to the attenuated lamps and stepping the dimming voltage from 10.0 to 5.0, 3.0, 2.0, and 1.6 V (Fig. S4). The $OH_{Oregon}$ experiment started with the non-attenuated lamps at 10V, then stepping the dimming voltage from 10.0 to 5.0 and 1.6 V. The OH exposure was calculated using Eq. (2) from Rowe et al. (2020):

$$\log[OH_{exp}] = \left(a + \left(b - c \times OHR_{ext}^d + e \times \log[O_3] \times OHR_{ext}^f\right) \times \log[O_3] + \log[H_2O]\right) + \log\left(\frac{\tau}{124}\right) \qquad (2)$$

Where $a$ through $f$ are fit coefficients tabulated in Table S2, $O_3$ is the ozone mixing ratio measured at the exit of the OFR (molec cm$^{-3}$), $OHR_{ext}$ is the external OH· reactivity (s$^{-1}$), which was calculated from the summed products of ambient VOC concentrations (measured with Vocus) and their and their OH· rate coefficients (see Data Availability section), $H_2O$ is the ambient water vapor mixing ratio (%), and $\tau$ is the residence time in the OFR. Corresponding calculated OH· exposures ranged from $3.91\times10^{11}$ to $2.53\times10^{12}$ molec cm$^{-3}$ s, or approximately 72 to 480 equivalent

7

hours (3 to 20 equivalent days) of atmospheric oxidation at a 24-hour average OH· concentration of $1.5 \times 10^6$ molec $cm^{-3}$ (Mao et al., 2009).

## 3 Results and Discussion

### 3.1 Ambient Organic Aerosol MAC(λ)

235 Table 1 summarizes the average MAC(λ) values ($m^2 g^{-1}$) of OA sampled from smoke plumes originating from the Arizona and Oregon wildfires. The absorption Ångström exponent (AAE), which parameterizes the wavelength dependence of absorption and is calculated from the two-parameter formula

$$AAE(488 \text{ nm}, 561 \text{ nm}) = -\frac{\ln\left[\frac{\beta_{abs}(488 \text{ nm})}{\beta_{abs}(561 \text{ nm})}\right]}{\ln\left[\frac{488 \text{ nm}}{561 \text{ nm}}\right]} \tag{3}$$

240 was $0.83 \pm 0.25$ in Arizona and $0.91 \pm 0.21$ in Oregon. As shown in Figs. S1 and S2, the rBC mass fraction in the sampled plumes were negligible (<5%) and within the margin of error due to charring of OA in the SP2 (Sedlacek et al, 2018). Therefore, we are confident that the calculated AAE values corresponded to light-absorbing OA constituents in the intercepted plumes.

**[Table 1]**

245 **3.2 NO₃· Oxidative aging of Organic Aerosol**

Equivalent nighttime oxidation of between $78.72 \pm 0.00$ to $184.08 \pm 4.03$ hours ($3.28 \pm 0.00$ to $7.67 \pm 0.17$ days) was performed across the NO$_{3,\text{Arizona}}$ and NO$_{3,\text{Oregon}}$ OFR experiments. Average surface wind speeds during these experiments were 0.39 m s$^{-1}$ in Arizona and 1.40 m s$^{-1}$ in Oregon. E$_{\text{MAC}}$(λ) is shown in Fig. 5 and summarized in Table 2, as the Oregon data points are obscured by their similarity. E$_{\text{MAC}}$(λ) from NO$_{3,\text{Arizona}}$ increases by a factor of up to

250 $1.69 \pm 0.38$ as a function of NO₃· exposure, as does E$_{\text{MAC}}$(λ) from NO$_{3,\text{Oregon}}$, although to a lesser extent because E$_{\text{MAC}}$(λ) was higher at lower equivalent time scales. There was a marked difference in the external reactivity (NO$_{3,\text{EXT}}$). NO$_{3,\text{EXT}}$ (and similarly, OH$_{\text{EXT}}$ in section 3.3) is the total summed reactivity of ambient gas-phase BBVOCs to NO₃ (or OH). Concentrations are measured by the PTR-MS during the ambient phases and calculated by NO$_{3,\text{EXT}}$ or OH$_{\text{EXT}}$ = $k_{\text{NO3 or OH}} \times$[NO₃ or OH]$\times$[BBVOC], where $k$ denotes the relevant rate constant. In Arizona,

255 calculated NO$_{3,\text{EXT}}$ values ranged from 11.6 to 17.6 s$^{-1}$, while in Oregon, NO$_{3\text{ext}}$ ranged from 161.0 to 187.1 s$^{-1}$; the NO₃· reactivity of catechol alone (measured by the PTR-MS) was 48 to 56 s$^{-1}$. This indicates the presence of high concentrations of biomass burning VOCs (BBVOCs)that were highly reactive to NO₃· (Finewax et al. 2017).

The differences in BBVOC external reactivities manifested in different E$_{\text{MAC}}$(λ) behavior at the two sites. On the shortest oxidation time scale in Arizona ($78.72 \pm 0.00$ equivalent hours), E$_{\text{MAC}}$(488 nm) was $0.99 \pm 0.26$ and E$_{\text{MAC}}$(561

260 nm) was $1.15 \pm 0.79$. This is in contrast to Oregon, where at $84.72 \pm 9.60$ equivalent hours, E$_{\text{MAC}}$(488 nm) was $1.47 \pm 0.01$ and E$_{\text{MAC}}$(561 nm) was $1.46 \pm 0.01$, which we attribute to the variations in BBVOC concentrations between sites. At longer time scales in Arizona, E$_{\text{MAC}}$ continued to increase, up to E$_{\text{MAC}}$(488 nm) of $1.69 \pm 0.38$ and E$_{\text{MAC}}$(561 nm)of $1.29 \pm 0.84$. These values were commensurate with results from Oregon at only $92.88 \pm 6.71$

equivalent hours. Regardless of choice of site, $E_{MAC}(\lambda)$ consistently increased with increasing $NO_3\cdot$ oxidation time
scales. Li et al. (2020) previously observed this absorption enhancement effect in the laboratory by subjecting biomass
burning BrC proxy aerosol derived from wood tar to a similar experimental setup to what was used here. They
observed $E_{MAC}(\lambda)$ in the near-UV (330-400 nm) of approximately 2.4, and approximately 6.0 in the visible (400-550
nm), though this high value comes from the ratio of two relatively low $MAC(\lambda)$ values of 0.6 and 0.1 $m^2$ $g^{-1}$, much
lower than the $MAC(561$ nm) reported here, which, for ambient aerosol was $1.71 \pm 0.32$ $m^2$ $g^{-1}$ in Arizona and $1.72 \pm 0.05$ $m^2$ $g^{-1}$ in Oregon.

[Figure 5]

[Table 2]

A breakdown of the chemical speciation from $NO_{3,Arizona}$ was obtained from the AMS data from before and after the
OFR_NO3_1 step (refer to Fig. S3), the first oxidation step after ozonolysis. During this step, 217 ppm $NO_2$ was
flowing into the LFR. $NO_{3,EXT}$ before and after this step was 17.56 and 13.90 $s^{-1}$, respectively, for an estimated
equivalent age of $138.24 \pm 5.23$ hours. The individual ions measured by the AMS can be visualized for oxidative
enhancement or depletion on a log-log scatterplot, shown with markers in Fig. S5, and with individual *m/z* in Fig. S6.
Ions above the solid black line are enhanced following $NO_3\cdot$ exposure, whereas ions below are depleted. The 2:1 and
1:2 lines are also included. Colors are per-ion family.

While knowledge of the individual *m/z* enhancement and depletion may inform future investigations, it is perhaps
more illustrative to consider ion families. Figure 6 shows the enhancement and depletion of the ion families in Figs.
S5 and S6 on the basis of total ion mass in that family. Enhancement is calculated by summing the relative abundances
of all ions within a family and taking the ratio of oxidized to ambient, similar to how $E_{MAC}(\lambda)$ is calculated.

[Figure 6]

The $CHO_{gt1}N$ ("$O_{gt1}$" indicates more than one oxygen atom in a molecule containing one or more atoms of C, H, and
N) family is enhanced by 211% and $CHO_1N$ ("$O_1$" indicates a single oxygen atom in a molecule containing one or
more atoms of C, H, and N) by 132% through the OFR, with a corresponding diminishment in $CHO_{gt1}$ and $CHO_1$
(where, again, "$O_{gt1}$" and "$O_1$" indicate the quantity of oxygen atoms in molecules of one or more atoms of C and H)
to 79% and 91%, respectively. This does not imply that all $CHO_1N$ species come from $CHO_1$ (or $CHO_{gt1}N$ from
$CHO_{gt1}$, similarly). The addition of nitrogen-containing functional groups is likely the cause of the observed light
absorption enhancement, since nitrogenated aromatic hydrocarbons form during reactions with $NO_3\cdot$ (Li et al., 2019)
and can act as chromophores, increasing light absorption (Jacobson, 1999; Laskin et al., 2015; Xie et al., 2019).

### 3.2.1 $O_3$ Oxidation Effects

The first step in the $NO_3\cdot$ experiments was an $O_3$-only oxidation experiment in case the effects of ozonolysis on
biomass burning smoke were significant. Since the $NO_3\cdot$ oxidation steps carry a significant amount of residual $O_3$, the
contribution of $O_3$ to changes in absorption behavior should be quantified and treated separately from $NO_3\cdot$. Li et al.
(2020) performed a similar experiment in their laboratory oxidation studies and found that $NO_3\cdot$ oxidation was the
dominant chemical transformation mechanism when compared to $O_3$. They further reported a slight decrease in
$MAC(405$ nm) quantified by a reduction in the imaginary refractive index from $0.017 \pm 0.005$ to $0.011 \pm 0.003$.

300    However, differences in how Li et al. performed their experiments (by exposing aerosol to 35 ppbv $O_3$ for 10.6 hours) preclude any direct comparison to the short $O_3$ exposure time scales performed during FIREX-AQ.

$E_{MAC}(\lambda)$ due to $O_3$ during $NO_{3,Arizona}$ was $1.06 \pm 0.96$ and $1.05 \pm 0.94$ for 488 and 561 nm, respectively, indicating that $O_3$ effects during the OFR experiments were negligible, or at least dominated by $NO_3\cdot$.

## 3.3 Daytime Oxidation

305    Compared to the $NO_3\cdot$ experiments, a much broader range of equivalent atmospheric aging was mimicked in the OH· experiments. $NO_3\cdot$ is a comparatively selective oxidant, while OH· tends to oxidize nearly all organic aerosol it comes in to contact with. Between approximately 72 and 480 equivalent hours (3 and 20 equivalent days) of oxidation were performed. Average surface wind speeds were 2.98 m s$^{-1}$ in Arizona and 0.43 m s$^{-1}$ in Oregon. As expected, $E_{MAC}(\lambda)$ for these experiments nominally showed light absorption diminishment for most experiments, however, $E_{MAC}(\lambda)$

310    exceeded unity between $91.06 \pm 1.30$ and $417.86 \pm 96.95$ hours. This effect of initial darkening and subsequent lightening has been reported previously (Sumlin et al., 2017a; Hems et al., 2020). The nature of this absorption enhancement mechanism was outside the scope of Sumlin et al. (2017) who rather focused on the likely mechanisms of BrC light diminishment, however Hems et al. (2020) posit that the increase in absorbance is linked to the formation of aromatic dimers and functionalization reactions. Hems et al. report that the absorption enhancement was observable

315    up to 11 equivalent hours of OH· exposure, and diminished with a net exposure of up to 42 hours. It should be noted that the samples analyzed by Hems et al. was only the water-soluble portion, obtained by gathering BrC on a filter and extracting with purified water. Furthermore, the OH· oxidation was carried out by adding hydrogen peroxide to the extract solution and exposing it to UV lamps. The OH· oxidation performed by the OFR during FIREX is far less controlled, given the dynamic nature of the plumes we sampled.

320    Figure 7 shows $E_{MAC}(\lambda)$ at 488 and 561 nm for all OH· experiments. The data is summarized in Table 3.

**[Figure 7]**

While $OH_{EXT}$ values were large, it is noteworthy that they were typically exceeded by $NO_{3,EXT}$ values, which, as noted in the previous section, indicates the presence of BBVOCs that are more reactive toward $NO_3\cdot$ than toward OH·. The

325    exact nature of these sensitivities requires further research.

**[Table 3]**

The same scatterplot analysis was applied to the OFR_1 step (refer to Fig. S4) of the $OH_{Arizona}$ experiment, however, it is less illustrative than with $NO_3\cdot$ because the primary driver of $MAC(\lambda)$ diminishment is fragmentation reactions.

330    Before this step, $OH_{EXT}$ was 74.95 s$^{-1}$ and after, it was 59.37 s$^{-1}$, giving an approximate equivalent age of $438.50 \pm 180.86$ hours. The enhancement ratios of the individual ion families show a decrease in $CHO_1N$ and an increase in $CHO_{gt1}N$, though to a lesser degree than under $NO_3\cdot$ aging. The ambient $CHO_{gt1}N$ mass fraction was approximately 25% higher in the $NO_{3,Arizona}$, as well – the comparatively lower relative abundances of nitroaromatics during $OH_{Arizona}$ (both pre- and post-OFR_1) may obfuscate any meaning in the enhancement ratios.

335   Figure S7 shows the OH$_{Arizona}$ scatterplot with markers, and Fig. S8 shows the individual *m/z* measured by the SP-AMS. Qualitatively, it can be observed that there is less spread in the scatterplot and the points are grouped closer to the 1:1 line, further suggesting that the dominant mechanism is fragmentation.

Figure 8 shows the ion family enhancement ratios through the same OFR_1 step corroborating the conclusions drawn from the scatterplots.

340                                        **[Figure 8]**


**4 Conclusions and Future Work - Synthesizing Daytime and Nighttime Aging**

The observations of E$_{MAC}(\lambda)$ and the associated chemistry of smoke OA sampled as part of the FIREX-AQ ground campaign represent the first attempt to use an OFR in a mobile setting to sample biomass burning at their source, as well as the first application of the novel MIPN v1 to a field study. Observations track closely with previous laboratory

345   studies.

These results show the difficulty in naïvely applying a particular aging model to atmospheric aerosol to constrain their long-term behavior in climate models. Aerosol does not age along any single pathway for more than half of a diurnal cycle: at night, oxidative aging of OA by NO$_3\cdot$ increases MAC$(\lambda)$, whereas daytime oxidative aging by OH$\cdot$ initially increases MAC$(\lambda)$, which is followed by a strong reduction in MAC$(\lambda)$ due to photobleaching. Overall, our results

350   suggest that explicit characterization of the effect of diel aging on atmospheric aerosol optical, chemical, and physical properties represents the best possible input to climate models.


**Data availability.** All experimental data, including MIPN; SP-AMS; SP2; and Vocus PTR-MS measurements, rate constants, and data tables used to calculate external reactivities are available for download at

355   doi:10.17632/5mr43vbks3.1 (Sumlin, 2021).


**Supplement.** Includes eight figures detailing rBC fraction observed during experiments (S1 and S2), sample timelines for oxidation experiments (S3 and S4), and AMS signal enhancements for various ion families upon oxidation (S5 through S8). Also includes two tables (S1 and S2) with fit coefficients for Eqs. (1) and (2).

360

**Author contributions.** RKC and BS conceived of the study and its design. RKC and AL provided guidance and supervision for carrying out the research tasks, interpretation of results, and contributed to the preparation of the manuscript. BS, EF, NJS, FM, CD, and SH performed the experiments. BS performed the data analysis, developed the figures, and led the preparation of the manuscript. All authors were involved in the editing and proofreading of the

365   manuscript.


**Competing interests**. The authors declare that they have no conflict of interest

**Acknowledgements**

375

## References

1. Arnott, W. P., Moosmüller, H., Rogers, F. C., Jin, T., and Bruch, R.: Photoacoustic spectrometer for measuring light absorption by aerosol: instrument description, Atmospheric Environment, 33, 2845-2852, 10.1016/s1352-2310(98)00361-6, 1999.

2. Arnott, W. P., Moosmüller, H., and Walker, J. W.: Nitrogen dioxide and kerosene-flame soot calibration of photoacoustic instruments for measurement of light absorption by aerosols, Review of Scientific Instruments, 71, 4545, 10.1063/1.1322585, 2000.

3. Atkinson, R.: Kinetics and Mechanisms of the Gas-Phase Reactions of the $NO_3$ Radical with Organic Compounds, J. Phys. Chem. Ref. Data 20, 20, 459-506, 10.1063/1.555887, 1991.

4. Canagaratna, M. R., Jayne, J. T., Jimenez, J. L., Allan, J. D., Alfarra, M. R., Zhang, Q., Onasch, T. B., Drewnick, F., Coe, H., Middlebrook, A., Delia, A., Williams, L. R., Trimborn, A. M., Northway, M. J., DeCarlo, P. F., Kolb, C. E., Davidovits, P., and Worsnop, D. R.: Chemical and microphysical characterization of ambient aerosols with the aerodyne aerosol mass spectrometer, Mass Spectrometry Reviews, 26, 185-222, 10.1002/mas.20115, 2007.

5. Carter, W., Luo, D., Malkina, I., and Pierce, J.: Environmental Chamber Studies of Atmospheric Reactivities of Volatile Organic Compounds: Effects of Varying Chamber and Light Source, Office of Scientific and Technical Information (OSTI), 1995.

6. Chakrabarty, R., Moosmüller, H., Chen, L.-W., Lewis, K., Arnott, W., Mazzoleni, C., Dubey, M., Wold, C., Hao, W., and Kreidenweis, S.: Brown carbon in tar balls from smoldering biomass combustion, Atmospheric Chemistry and Physics, 10, 6363-6370, 2010.

7. Cheng, Z., Atwi, K. M., Yu, Z., Avery, A., Fortner, E. C., Williams, L., Majluf, F., Krechmer, J. E., Lambe, A. T., and Saleh, R.: Evolution of the light-absorption properties of combustion brown carbon aerosols following reaction with nitrate radicals, Aerosol Science and Technology, 54, 849-863, 10.1080/02786826.2020.1726867, 2020.

8. Cocker, D. R., Flagan, R. C., and Seinfeld, J. H.: State-of-the-Art Chamber Facility for Studying Atmospheric Aerosol Chemistry, Environmental Science & Technology, 35, 2594-2601, 10.1021/es0019169, 2001.

9. Cubison, M. J., Ortega, A. M., Hayes, P. L., Farmer, D. K., Day, D., Lechner, M. J., Brune, W. H., Apel, E., Diskin, G. S., Fisher, J. A., Fuelberg, H. E., Hecobian, A., Knapp, D. J., Mikoviny, T., Riemer, D., Sachse, G. W., Sessions, W., Weber, R. J., Weinheimer, A. J., Wisthaler, A., and Jimenez, J. L.: Effects of aging on organic aerosol from open biomass burning smoke in aircraft and laboratory studies, Atmos. Chem. Phys., 11, 12049-12064, 10.5194/acp-11-12049-2011, 2011.

10. Finewax, Z., de Gouw, J. A., and Ziemann, P. J.: Identification and Quantification of 4-Nitrocatechol Formed from OH and $NO_3$ Radical-Initiated Reactions of Catechol in Air in the Presence of $NO_X$: Implications for Secondary Organic Aerosol Formation from biomass Burning, Environmental Science & Technology, 52, 1981-1989, 10.1021/acs.est.7b05864, 2018.

11. Grieshop, A. P., Logue, J. M., Donahue, N. M., and Robinson, A. L.: Laboratory investigation of photochemical oxidation of organic aerosol from wood fires 1: measurement and simulation of organic aerosol evolution, Atmospheric Chemistry and Physics, 9, 1263-1277, 10.5194/acp-9-1263-2009, 2009.

12. He, Q., Tomaz, S., Li, C., Zhu, M., Meidan, D., Riva, M., Laskin, A., Brown, S. S., George, C., Wang, X., and Rudich, Y.: Optical Properties of Secondary Organic Aerosol Produced by Nitrate Radical Oxidation of Biogenic Volatile Organic Compounds, Environmental Science & Technology, 55, 2878-2889, 10.1021/acs.est.0c06838, 2021.

13. Hems, R. F., Schnitzler, E. G., Bastawrous, M., Soong, R., Simpson, A. J., and Abbatt, J. P. D.: Aqueous Photoreactions of Wood Smoke Brown Carbon, ACS Earth and Space Chemistry, 4, 1149-1160, 10.1021/acsearthspacechem.0c00117, 2020.

14. Jacobson, M. Z.: Isolating nitrated and aromatic aerosols and nitrated aromatic gases as sources of ultraviolet light absorption, Journal of Geophysical Research: Atmospheres, 104, 3527-3542, 10.1029/1998jd100054, 1999.

15. Jayne, J. T., Leard, D. C., Zhang, X., Davidovits, P., Smith, K. A., Kolb, C. E., and Worsnop, D. R.: Development of an Aerosol Mass Spectrometer for Size and Composition Analysis of Submicron Particles, Aerosol Science and Technology, 33, 49-70, 10.1080/027868200410840, 2000.

16. Jimenez, J. L., Canagaratna, M., Donahue, N., Prevot, A., Zhang, Q., Kroll, J. H., DeCarlo, P. F., Allan, J. D., Coe, H., and Ng, N.: Evolution of organic aerosols in the atmosphere, science, 326, 1525-1529, 2009.

17. Krechmer, J., Lopez-Hilfiker, F., Koss, A., Hutterli, M., Stoermer, C., Deming, B., Kimmel, J., Warneke, C., Holzinger, R., Jayne, J., Worsnop, D., Fuhrer, K., Gonin, M., and de Gouw, J.: Evaluation of a New Reagent-Ion Source and Focusing Ion–Molecule Reactor for Use in Proton-Transfer-Reaction Mass Spectrometry, Analytical Chemistry, 90, 12011-12018, 10.1021/acs.analchem.8b02641, 2018.

18. Kroll, J. H., Donahue, N. M., Jimenez, J. L., Kessler, S. H., Canagaratna, M. R., Wilson, K. R., Altieri, K. E., Mazzoleni, L. R., Wozniak, A. S., and Bluhm, H.: Carbon oxidation state as a metric for describing the chemistry of atmospheric organic aerosol, Nature Chemistry, 3, 133, 2011.

19. Lambe, A. T., Ahern, A. T., Williams, L. R., Slowik, J. G., Wong, J. P. S., Abbatt, J. P. D., Brune, W. H., Ng, N. L., Wright, J. P., Croasdale, D. R., Worsnop, D. R., Davidovits, P., and Onasch, T. B.: Characterization of aerosol photooxidation flow reactors: heterogeneous oxidation, secondary organic aerosol formation and cloud condensation nuclei activity measurements, Atmospheric Measurement Techniques, 4, 445-461, 10.5194/amt-4-445-2011, 2011.

20. Lambe, A. T., Cappa, C. D., Massoli, P., Onasch, T. B., Forestieri, S. D., Martin, A. T., Cummings, M. J., Croasdale, D. R., Brune, W. H., and Worsnop, D. R.: Relationship between oxidation level and optical properties of secondary organic aerosol, Environmental science & technology, 47, 6349-6357, 2013.

21. Lambe, A. T., Wood, E. C., Krechmer, J. E., Majluf, F., Williams, L. R., Croteau, P. L., Cirtog, M., Féron, A., Petit, J.-E., Albinet, A., Jimenez, J. L., and Peng, Z.: Nitrate radical generation via continuous generation of dinitrogen pentoxide in a laminar flow reactor coupled to an oxidation flow reactor, Atmospheric Measurement Techniques, 13, 2397-2411, 10.5194/amt-13-2397-2020, 2020.

22. Laskin, A., Laskin, J., and Nizkorodov, S. A.: Chemistry of atmospheric brown carbon, Chemical reviews, 115, 4335-4382, 2015.

23. Lewis, K., Arnott, W. P., Moosmüller, H., and Wold, C. E.: Strong spectral variation of biomass smoke light absorption and single scattering albedo observed with a novel dual-wavelength photoacoustic instrument, Journal of Geophysical Research: Atmospheres, 113, 2008.

24. Li, C., He, Q., Hettiyadura, A. P. S., Käfer, U., Shmul, G., Meidan, D., Zimmermann, R., Brown, S. S., George, C., Laskin, A., and Rudich, Y.: Formation of Secondary Brown Carbon in Biomass Burning Aerosol Proxies through $NO_3$ Radical Reactions, Environmental Science & Technology, 54, 1395-1405, 10.1021/acs.est.9b05641, 2019.

25. Li, C., He, Q., Fang, Z., Brown, S. S., Laskin, A., Cohen, S. R., and Rudich, Y.: Laboratory Insights into the Diel Cycle of Optical and Chemical Transformations of Biomass Burning Brown Carbon Aerosols, Environmental Science & Technology, 54, 11827-11837, 10.1021/acs.est.0c04310, 2020.

26. Li, Q., Jacob, D. J., Bey, I., Yantosca, R. M., Zhao, Y., Kondo, Y., and Notholt, J.: Atmospheric hydrogen cyanide (HCN): Biomass burning source, ocean sink?, Geophysical Research Letters, 27, 357-360, 10.1029/1999gl010935, 2000.

27. Mao, J., Ren, X., Brune, W. H., Olson, J. R., Crawford, J. H., Fried, A., Huey, L. G., Cohen, R. C., Heikes, B., Singh, H. B., Blake, D. R., Sachse, G. W., Diskin, G. S., Hall, S. R., and Shetter, R. E.: Airborne measurement of OH reactivity during INTEX-B, Atmospheric Chemistry and Physics, 9, 163-173, 10.5194/acp-9-163-2009, 2009.

28. McClure, C. D., and Jaffe, D. A.: US particulate matter air quality improves except in wildfire-prone areas, Proc Natl Acad Sci U S A, 115, 7901-7906, 10.1073/pnas.1804353115, 2018.

29. McManus, J. B., Zahniser, M. S., and Nelson, D. D.: Dual quantum cascade laser trace gas instrument with astigmatic Herriott cell at high pass number, Appl. Opt., 50, A74-A85, 10.1364/AO.50.000A74, 2011a.

30. McManus, J. B., Zahniser, M. S., Nelson, D. D., McGovern, R. M., Agnese, M., and Brown, W. F.: Compact Quantum Cascade Laser Instrument for High Precision Trace Gas Measurements, in: OSA Technical Digest (CD), Renewable Energy and the Environment, Austin, Texas, 2011b, EThC2,

31. McMurry, P. H., and Grosjean, D.: Gas and aerosol wall losses in Teflon film smog chambers, Environmental Science & Technology, 19, 1176-1182, 10.1021/es00142a006, 1985.

32. Mitroo, D., Sun, Y., Combest, D., Kumar, P., and Williams, B.: Assessing the degree of plug flow in oxidation flow reactors (OFRs): a study on a potential aerosol mass (PAM) reactor, Atmospheric Measurement Techniques, 11, 1741-1756, 10.5194/amt-11-1741-2018, 2018.

33. Moosmüller, H., and Arnott, W. P.: Angular truncation errors in integrating nephelometry, Review of Scientific Instruments, 74, 3492-3501, 10.1063/1.1581355, 2003.

34. Murphy, D. M., Cziczo, D. J., Froyd, K. D., Hudson, P. K., Matthew, B. M., Middlebrook, A. M., Peltier, R. E., Sullivan, A., Thomson, D. S., and Weber, R. J.: Single-particle mass spectrometry of tropospheric aerosol particles, Journal of Geophysical Research: Atmospheres, 111, 10.1029/2006jd007340, 2006.

35. Onasch, T. B., Trimborn, A., Fortner, E. C., Jayne, J. T., Kok, G. L., Williams, L. R., Davidovits, P., and Worsnop, D. R.: Soot Particle Aerosol Mass Spectrometer: Development, Validation, and Initial Application, Aerosol Science and Technology, 46, 804-817, 10.1080/02786826.2012.663948, 2012.

36. Ortega, A. M., Day, D. A., Cubison, M. J., Brune, W. H., Bon, D., de Gouw, J. A., and Jimenez, J. L.: Secondary organic aerosol formation and primary organic aerosol oxidation from biomass-burning smoke in a flow reactor during FLAME-3, Atmospheric Chemistry and Physics, 13, 11551-11571, 10.5194/acp-13-11551-2013, 2013.

37. Palm, B. B., Campuzano-Jost, P., Day, D. A., Ortega, A. M., Fry, J. L., Brown, S. S., Zarzana, K. J., Dube, W., Wagner, N. L., Draper, D. C., Kaser, L., Jud, W., Karl, T., Hansel, A., Gutiérrez-Montes, C., and Jimenez, J. L.: Secondary organic aerosol formation from in situ OH, O3, and NO3 oxidation of ambient forest air in an oxidation flow reactor, Atmos. Chem. Phys., 17, 5331-5354, 10.5194/acp-17-5331-2017, 2017.

38. Pierce, J. R., Engelhart, G. J., Hildebrandt, L., Weitkamp, E. A., Pathak, R. K., Donahue, N. M., Robinson, A. L., Adams, P. J., and Pandis, S. N.: Constraining Particle Evolution from Wall Losses, Coagulation, and Condensation-Evaporation in Smog-Chamber Experiments: Optimal Estimation Based on Size Distribution Measurements, Aerosol Science and Technology, 42, 1001-1015, 10.1080/02786820802389251, 2008.

39. Pósfai, M., Gelencsér, A., Simonics, R., Arató, K., Li, J., Hobbs, P. V., and Buseck, P. R.: Atmospheric tar balls: Particles from biomass and biofuel burning, Journal of Geophysical Research: Atmospheres, 109, 2004.

40. Riccardi, C. L., Ottmar, R. D., Sandberg, D. V., Andreu, A., Elman, E., Kopper, K, and Long, J.: The fuelbed: a key element of the Fuel Characteristic Classification System, Canadian Journal of Forest Research 37, 2394-2412, 10.1139/X07-143, 2007.

41. Rowe, J. P., Lambe, A. T., and Brune, W. H.: Technical Note: Effect of varying the $\lambda = 185$ and 254 nm photon flux ratio on radical generation in oxidation flow reactors, Atmos. Chem. Phys. Discuss., 2020, 1-15, 10.5194/acp-2020-642, 2020.

42. Sedlacek, A. J., Onasch, T. B., Nichman, L., Lewis, E. R., Davidovits, P, Freedman, A., and Williams, L.: Formation of refractory black carbon by SP2-induced charring of organic aerosol, Aerosol Sci. & Tech, 52:12, 1345-1350, DOI: 10.1080/02786826.2018.1531107, 2018.

43. Stein, A. F., Draxler, R. R., Rolph, G. D., Stunder, B. J. B., Cohen, M. D., and Ngan, F.: NOAA's HYSPLIT Atmospheric Transport and Dispersion Modeling System, Bulletin of the American Meteorological Society, 96, 2059-2077, 10.1175/bams-d-14-00110.1, 2016.

44. Stephens, M., Turner, N., and Sandberg, J.: Particle identification by laser-induced incandescence in a solid-state laser cavity, Appl. Opt., 42, 3726-3736, 10.1364/AO.42.003726, 2003.

14

45. Sumlin, Benjamin (2021), "OH and NO3 Oxidation Data from FIREX-AQ Ground Experiments", Mendeley Data, V1, doi: 10.17632/5mr43vbks3.1.

500 46. Sumlin, B. J., Pandey, A., Walker, M. J., Pattison, R. S., Williams, B. J., and Chakrabarty, R. K.: Atmospheric photooxidation diminishes light absorption by primary brown carbon aerosol from biomass burning, Environmental Science & Technology Letters, 4, 540-545, 2017a.

47. Sumlin, B. J., Pandey, A., Walker, M. J., Pattison, R. S., Williams, B. J., and Chakrabarty, R. K.: Atmospheric Photooxidation Diminishes Light Absorption by Primary Brown Carbon Aerosol from Biomass Burning, Environ. Sci. Technol. Lett., 4, 540, 505 2017b.

48. Sumlin, B. J., Heinson, Y. W., Shetty, N., Pandey, A., Pattison, R. S., Baker, S., Hao, W. M., and Chakrabarty, R. K.: UV–Vis–IR spectral complex refractive indices and optical properties of brown carbon aerosol from biomass burning, Journal of Quantitative Spectroscopy and Radiative Transfer, 206, 392-398, 2018a.

49. Sumlin, B. J., Oxford, C. R., Seo, B., Pattison, R. R., Williams, B. J., and Chakrabarty, R. K.: Density and Homogeneous 510 Internal Composition of Primary Brown Carbon Aerosol, Environmental Science & Technology, 52, 3982-3989, 10.1021/acs.est.8b00093, 2018b.

50. Varma, R., Moosmüller, H., and Arnott, W. P.: Toward an ideal integrating nephelometer, Optics Letters, 28, 1007, 10.1364/ol.28.001007, 2003.

51. Wang, N., Jorga, S. D., Pierce, J. R., Donahue, N. M., and Pandis, S. N.: Particle wall-loss correction methods in smog chamber 515 experiments, Atmospheric Measurement Techniques, 11, 6577-6588, 10.5194/amt-11-6577-2018, 2018.

52. Warneke, C. S., Joshua; Ryerson, Tom; Crawford, James; Dibb, Jack; Lefer, Barry; Roberts, James; Trainer, Michael; Murphy, Daniel; Brown, Steven; Brewer, Alan; Gao, Ru-Shan; Fahey, David: Fire Influence on Regional to Global Environments and Air Quality (FIREX-AQ), in preparation.

53. Xie, M., Chen, X., Hays, M. D., and Holder, A. L.: Composition and light absorption of N-containing aromatic compounds in 520 organic aerosols from laboratory biomass burning, Atmospheric Chemistry and Physics, 19, 2899-2915, 2019.

54. Zhang, Q., Jimenez, J. L., Canagaratna, M., Allan, J., Coe, H., Ulbrich, I., Alfarra, M., Takami, A., Middlebrook, A., and Sun, Y.: Ubiquity and dominance of oxygenated species in organic aerosols in anthropogenically-influenced Northern Hemisphere midlatitudes, Geophysical Research Letters, 34, 2007.

55. Zhang, X., Cappa, C. D., Jathar, S. H., McVay, R. C., Ensberg, J. J., Kleeman, M. J., and Seinfeld, J. H.: Influence of vapor 525 wall loss in laboratory chambers on yields of secondary organic aerosol, Proceedings of the National Academy of Sciences, 111, 5802-5807, 10.1073/pnas.1404727111, 2014.
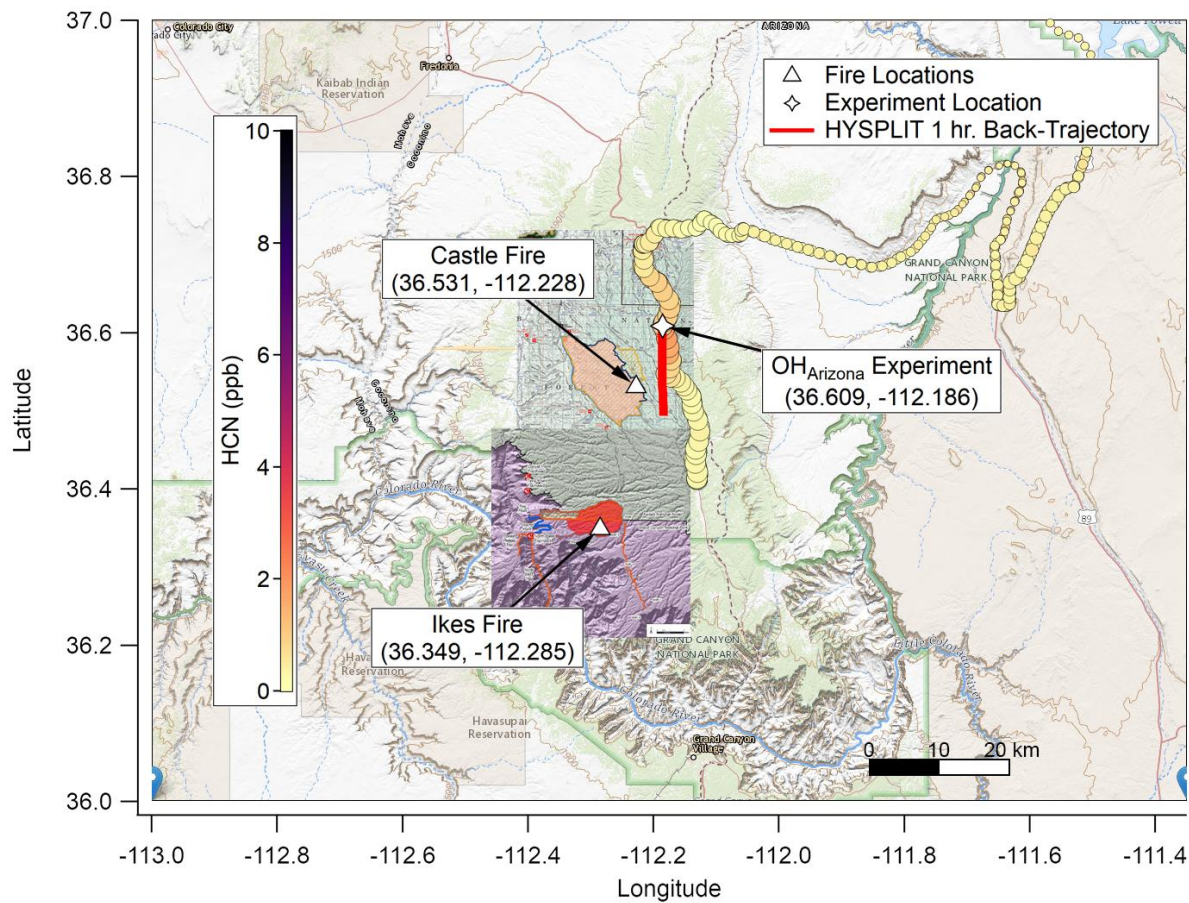
**Figures and Tables**

**Figure 1: Map of the Grand Canyon region overlaid with HCN concentration (ppb, color scale), elevation (HCN marker size, larger is higher AMSL), fire origin locations from Incident Information System (white triangles), OH$_{Arizona}$ experiment location (white star), and fire boundary maps for 08/20/2019. Based on HYSPLIT back-trajectories, the plume for this experiment was less than one hour old, though surface concentrations of smoke were comparatively lower since the nocturnal boundary layer had lifted. Background map is from USGS EarthExplorer, and fire map overlays are from the National Wildfire Coordinating Group's Incident Information System (InciWeb).**
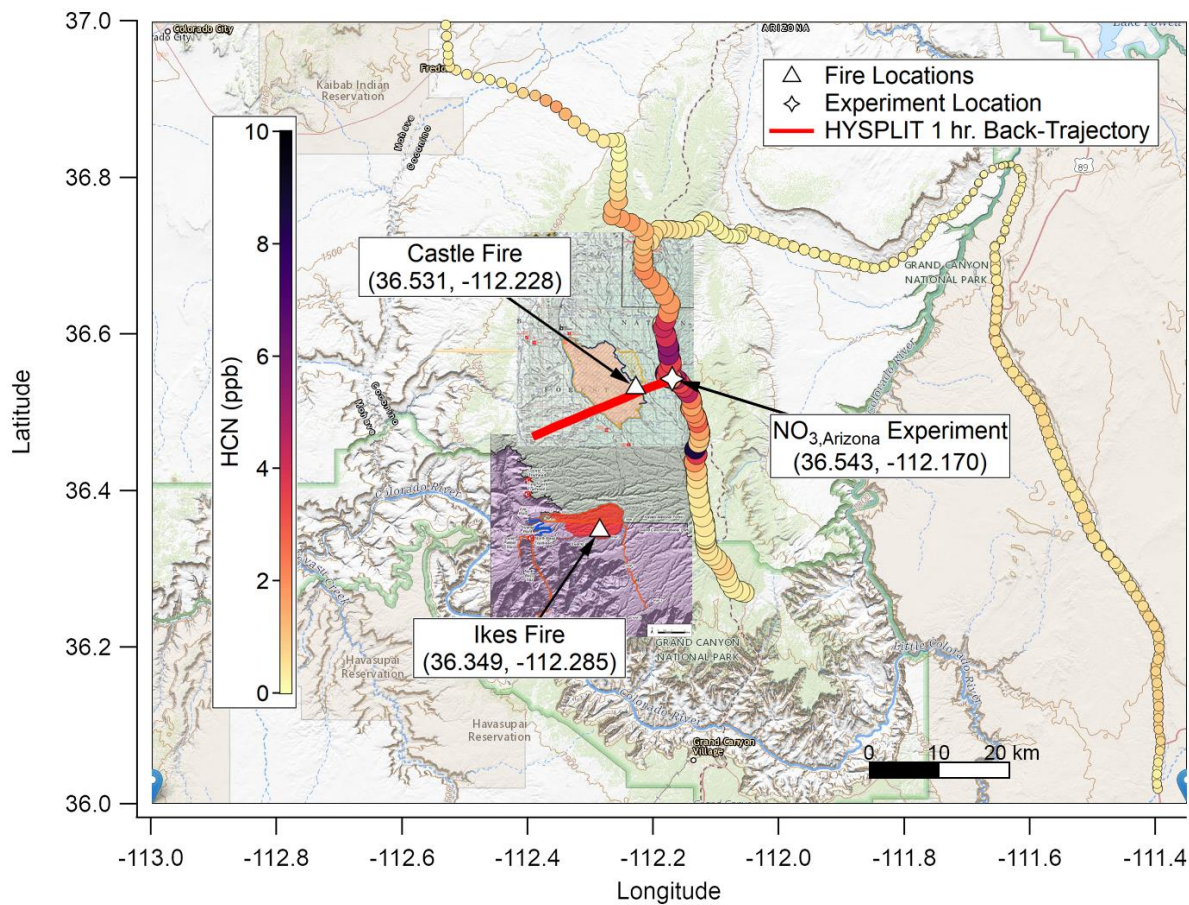
**Figure 2: As with Figure 2, but for NO$_{3,\text{Arizona}}$ on 08/22/2019. Based on HYSPLIT back-trajectories, the plume for this experiment was again less than one hour old, though smoke that had settled in the valley under the nocturnal boundary layer may have been older. Background map is from USGS EarthExplorer, and fire map overlays are from the National Wildfire Coordinating Group's Incident Information System (InciWeb).**
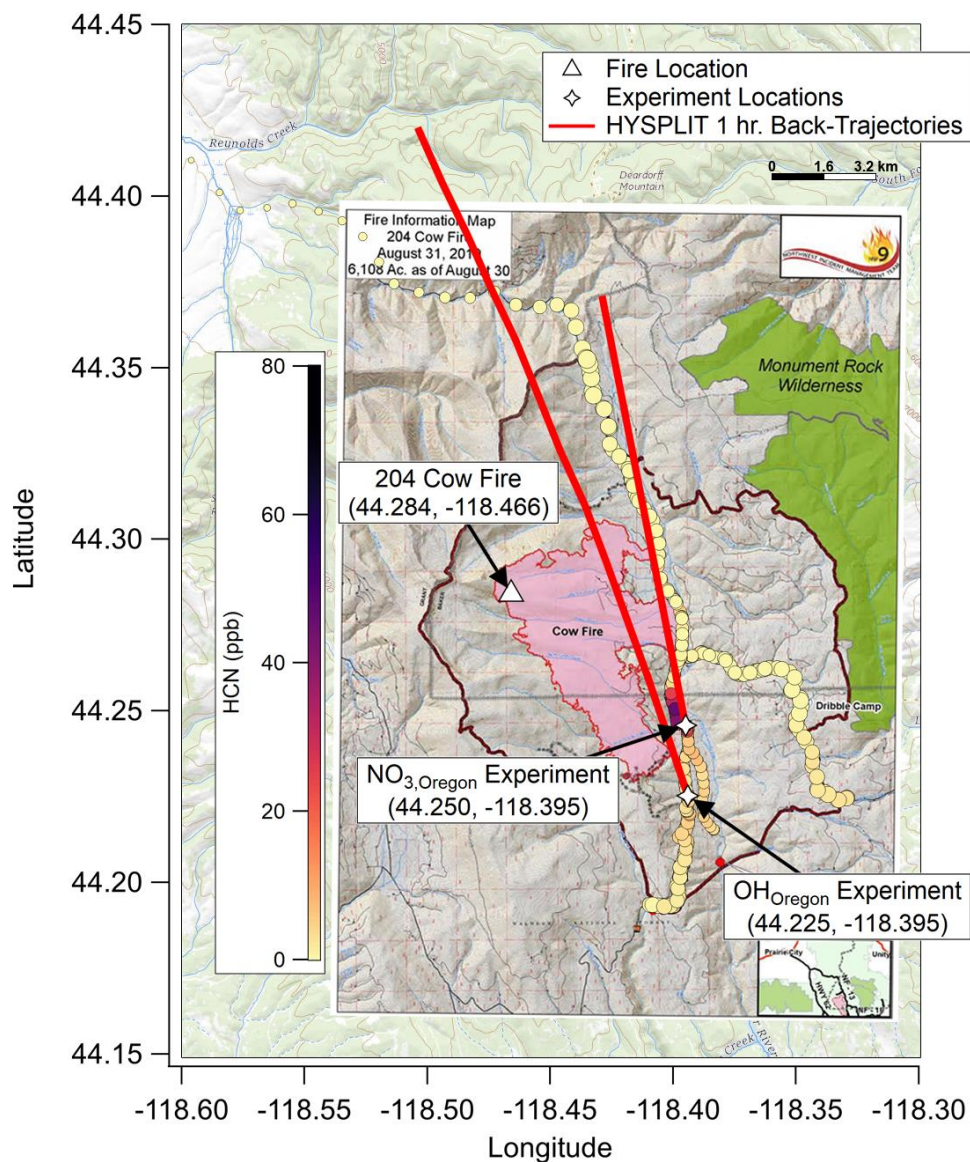
**Figure 3: As with Figures 2 and 3, showing fire ignition point (white triangle), OH<sub>Oregon</sub> and NO3<sub>,Oregon</sub> experiment locations (white stars), and fire boundary maps for 08/26/2019. HYSPLIT back-trajectories again show the plumes for these experiments were much less than one hour old. Background map is from USGS EarthExplorer, and fire map overlays are from the National Wildfire Coordinating Group's Incident Information System (InciWeb).**
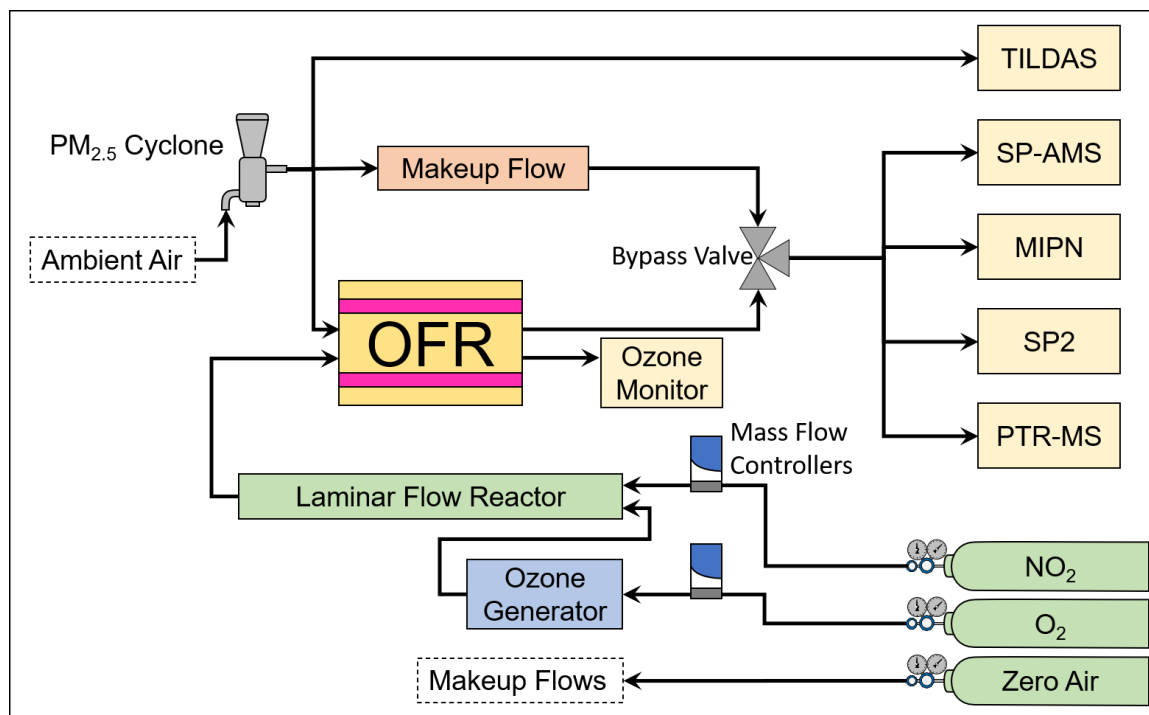
545

**Figure 4: A schematic of the general experimental setup aboard the AML showing instruments, reactors, reagents, and other hardware.**

550



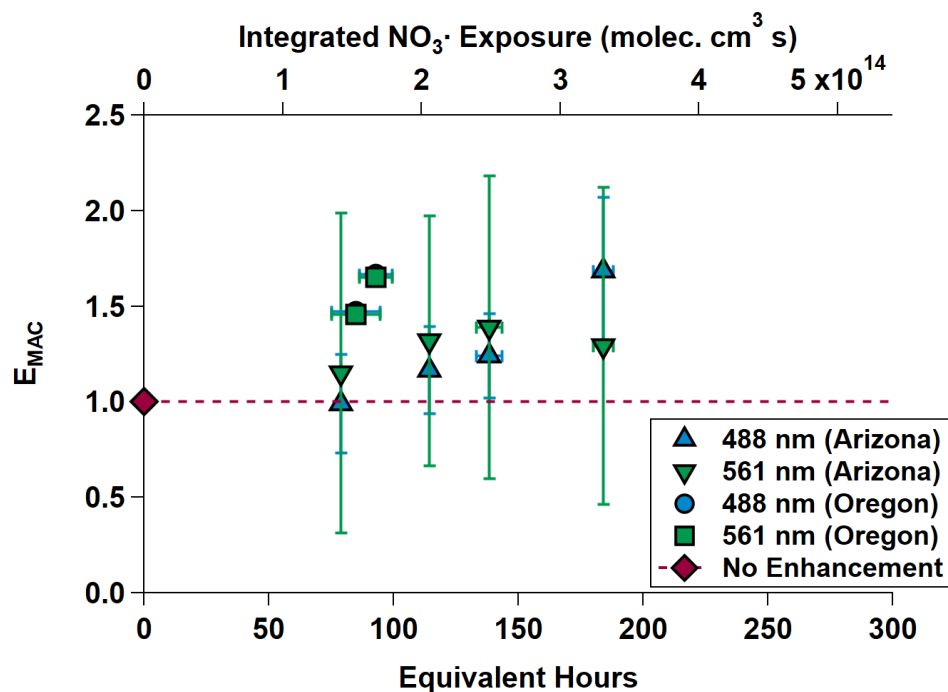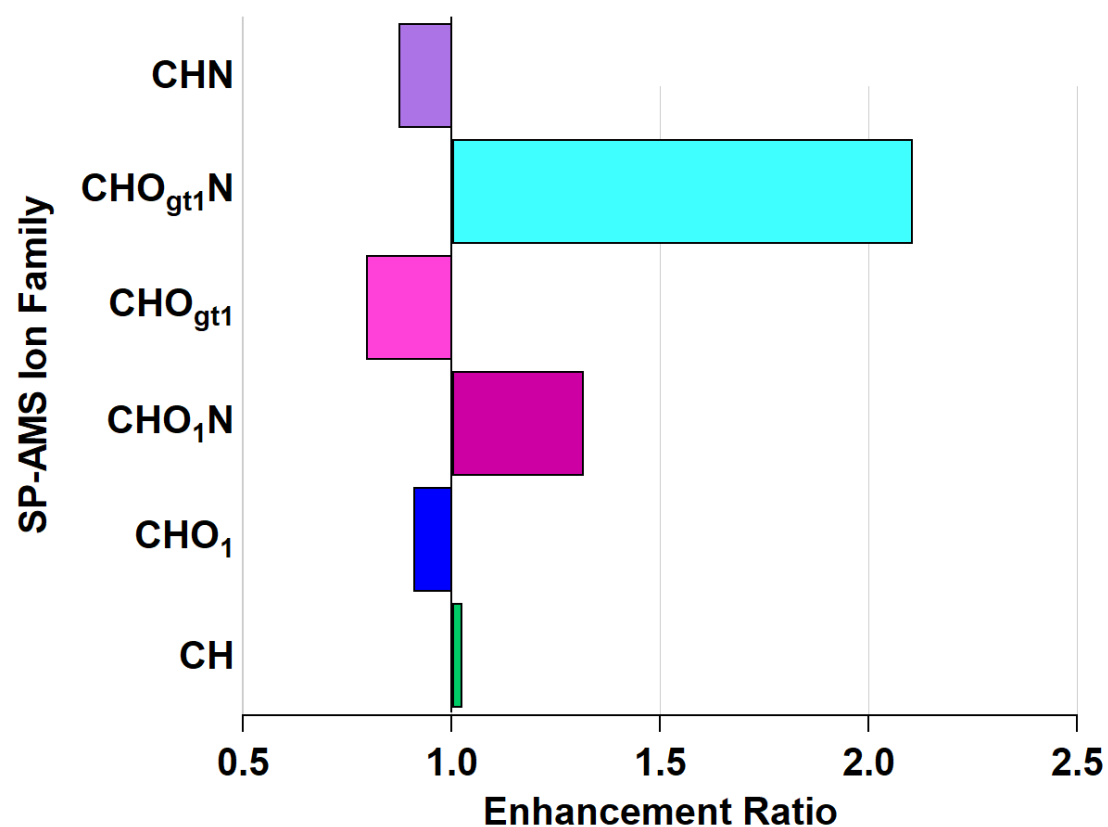**Figure 5: MAC(λ) Enhancements at 488 and 561 nm during $NO_{3,Arizona}$ (triangles) and $NO_{3,Oregon}$ (square and circle; the circle is partially obscured by the square). The gray dashed line is the "no enhancement" line. The Arizona experiment data shows an increasing trend in MAC(λ) with increasing equivalent age. The Oregon data on its own does, as well, but in**

555

context of the Arizona data, the chemical species present in the smoke plume in Oregon appear to have been much more reactive towards $NO_3\cdot$. Equivalent photochemical age is calculated from the $NO_3\cdot$ exposure in the OFR and assuming an average ambient $NO_3\cdot$ concentration of $5\times10^8$ molec cm$^{-3}$ (Atkinson et al, 1991).



Figure 6: Enhancement and depletion of ion families measured by the AMS during $NO_3\cdot$ oxidation. $CHO_1N$ and $CHO_{gt1}N$, while present in lower relative abundances, showed the largest enhancement through $NO_3\cdot$ oxidation.

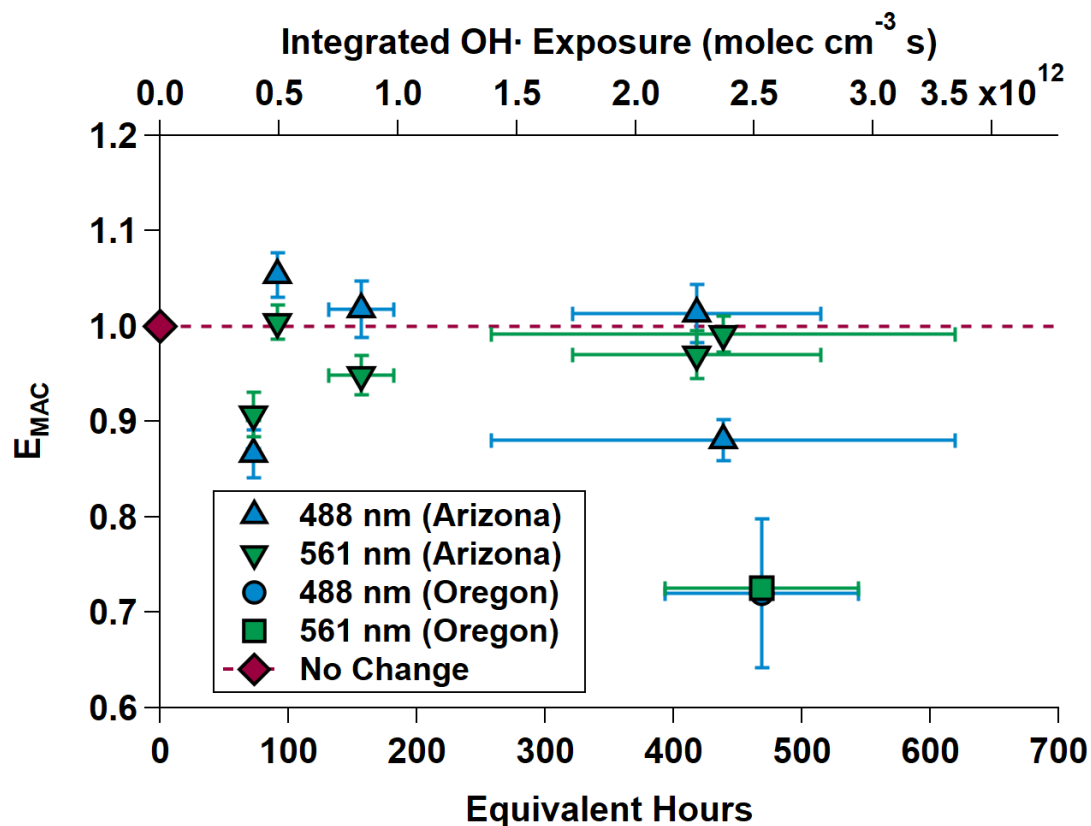**Figure 7: MAC(λ) Enhancements at 488 and 561 nm during OH$_{Arizona}$ (triangles) and OH$_{Oregon}$ (square and circle, which is partially obscured). The gray dashed line is the "no enhancement" line. The shows an initial diminishment, then subsequent increasing to decreasing trend in MAC(λ) with increasing equivalent age. Equivalent photochemical age (hours) is calculated from the OH· exposure in the OFR and assuming an average ambient OH· concentration of 1.5×10$^6$ molec cm$^{-3}$ (Mao et al, 2009).**
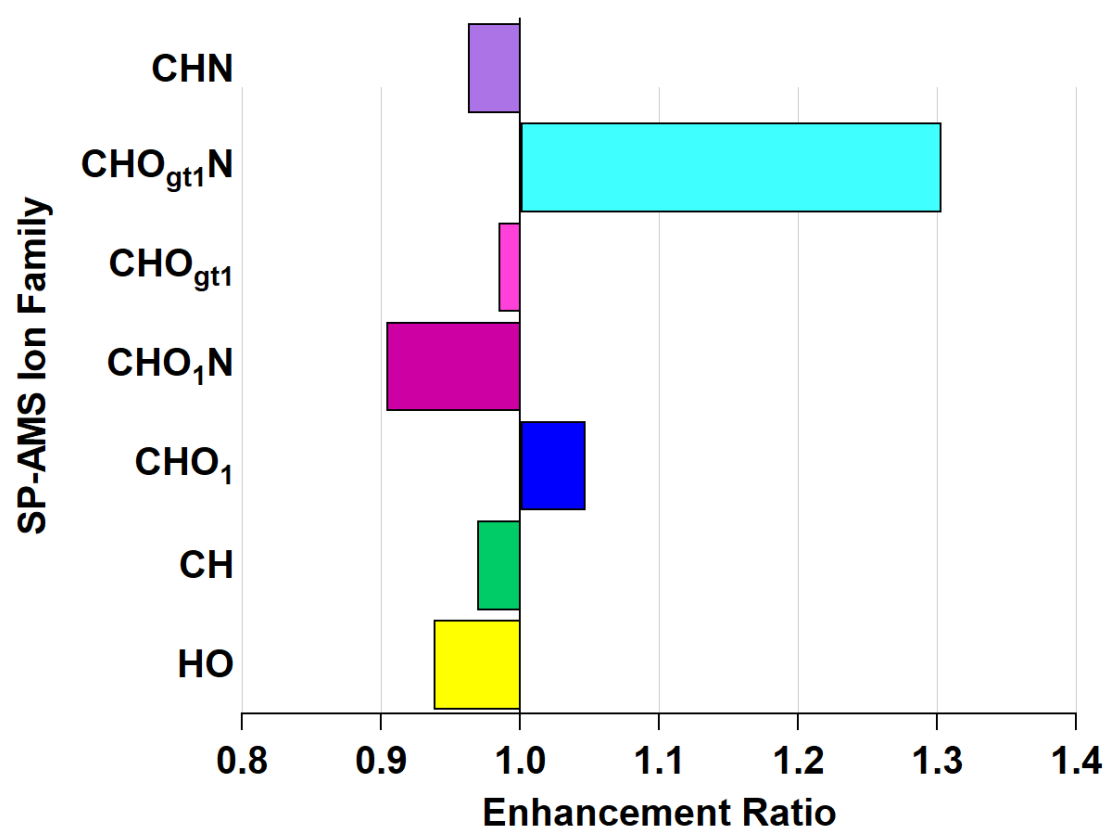
**Figure 8: Enhancement and depletion of ion families measured by the AMS during OH· oxidation. $CHO_1N$ is depleted while $CHO_{gt1}N$ is enhanced, however, both these families are present in low relative abundances which may exaggerate the enhancement ratio.**

570

**Table 1: Study-average values of mass absorption coefficients (MAC, m2 g-1) from Arizona and Oregon. Errors are one standard deviation.**

| Wavelength | Arizona MAC | Oregon MAC |
|---|---|---|
| 488 nm | $1.93 \pm 0.33$ | $1.95 \pm 0.41$ |
| 561 nm | $1.71 \pm 0.32$ | $1.72 \pm 0.05$ |

**Table 2: $E_{MAC}$(488 nm) and $E_{MAC}$(561 nm) for NO$_3$· oxidation experiments. Asterisks denote NO$_{3,Oregon}$. All others taken during NO$_{3,Arizona}$, and the dagger indicates O$_3$-only oxidation.**

| Equivalent hours | $E_{MAC}$ at $\lambda$ = 488 nm | $E_{MAC}$ at $\lambda$ = 561 nm |
|---|---|---|
| $78.72 \pm 0.00$ | $0.99 \pm 0.26$ | $1.15 \pm 0.79$ |
| $84.72 \pm 9.60$* | $1.47 \pm 0.01$ | $1.46 \pm 0.01$ |
| $92.88 \pm 6.71$* | $1.67 \pm 0.01$ | $1.65 \pm 0.01$ |
| $114.24 \pm 0.00$ | $1.17 \pm 0.23$ | $1.32 \pm 0.66$ |
| $138.24 \pm 5.23$ | $1.24 \pm 0.22$ | $1.39 \pm 0.79$ |
| $184.08 \pm 4.03$ | $1.69 \pm 0.38$ | $1.29 \pm 0.84$ |
| n/a[†] | $1.06 \pm 0.96$ | $1.05 \pm 0.94$ |

**Table 3: $E_{MAC}$(488 nm) and $E_{MAC}$(561 nm) for OH· oxidation experiments. Asterisk denotes OH$_{Oregon}$. All others taken during OH$_{Arizona}$.**

| Equivalent hours | $E_{MAC}$ at $\lambda$ = 488 nm | $E_{MAC}$ at $\lambda$ = 561 nm |
|---|---|---|
| $72.50 \pm 4.83$ | $0.88 \pm 0.02$ | $0.94 \pm 0.02$ |
| $91.06 \pm 1.30$ | $1.05 \pm 0.02$ | $1.00 \pm 0.02$ |
| $156.36 \pm 25.45$ | $1.02 \pm 0.03$ | $0.95 \pm 0.02$ |
| $417.86 \pm 96.95$ | $1.02 \pm 0.03$ | $0.97 \pm 0.03$ |
| $438.50 \pm 180.86$ | $0.88 \pm 0.02$ | $0.99 \pm 0.02$ |
| $468.54 \pm 75.36$* | $0.72 \pm 0.08$ | $0.73 \pm 0.01$ |